Natural Resources for Human Health

eISSN: 2583-1194

Original Research

Received 24 July 2026
Revised 28 Aug 2026
Accepted 12 Sep 2026

Natural Resources for Human Health 2026, Vol.6(22s): 914–928

KEYWORDS:
Auto combustion, green fuel, XRD, band gap, Photodegradation.

Green Synthesis of Sm Doped SrFe12O19 using Buteamonosperma leaf: Photodegradation

K. M. Pooja[1], G. Y. Akarsh[2], H. A. Anilkumara[2], N. K. Vasantakumarnaik[3], T. Ravikumar Naik[4], P. Parameshwara Naik[1*], G. Krishnamurthy[2]

[1]Department of PG Studies and Research in Chemistry, Sahyadri Science College, Kuvempu University, Shivamogga, Karnataka, India-577203
[2]Department of PG Studies and Research in Industrial Chemistry, Sahyadri Science College, Kuvempu University, Shivamogga, Karnataka, India-577203
[3]Department of Studies and Research in Chemistry, University College of Science, Tumkur University, Tumkur, Karnataka, India-572103
[4]Department of PG Studies in Chemistry, Veerashaiva College, Vijayanagara Sri Krishnadevaraya University, Ballari, Karnataka, India-583105

ABSTRACT: Rare-earth doped strontium hexaferrites ($SrFe_{12}O_{19}$) synthesized via auto combustion using Buteamonosperma (BMS) leaf as a green fuel. Samarium (Sm) doped $SrFe_{12}O_{19}$ were analyzed using FTIR, UV-Visible spectroscopy, SEM, TEM, energy-dispersive X-ray analysis (EDX). The XRD results showed predominantly hexagonal magnetoplumbite phase. Optical analysis revealed the band gap of approximately 3.35eV. Photodegradation of the synthesized materials was investigated under natural sunlight on different organic dyes as model pollutants. Among the tested compounds, 5% Sm doped $SrFe_{12}O_{19}$ demonstrated the highest degradation efficiency on methylene blue (MB) dye.

1. INTRODUCTION

Strontium hexaferrites are known for their environmental, electrical and technical applications. Many of them are used as electrochemical sensors, in photo-catalysis, electric motors, loud speakers, high-frequency devices and magnetic recorder. The properties of these nanomaterials depend on their structure and orientation of atomic arrangement. M-type hexagonal ferrites found to possess a layered crystal arrangement comprising alternating spinel and R structural blocks [1- 3]. They gain high phase stability, adaptable chemical composition and durable crystal framework etc, Doping rare earth can effectively tailor the physical, structural and electrical properties to meet modern technological requirements [4]. In rare earth elements, due to the presence of 4f electrons, widely recognized for their unique optical and electronic properties and make them essential in advanced technologies such as electronic devices, laser systems, permanent magnets and superconducting materials. Thus, introducing rare earth metals into the strontium hexaferrites lattices significantly modify the electrical, magnetic and photocatalytic properties [5-7]. Conventional preparation of ferrites commonly involves solid state reactions followed by mechanical ball milling to achieve fine powders [8]. However, prolonged milling can introduce internal strain, irregular particle morphology and partial demagnetization which may degrade magnetic performance [9]. To overcome these drawbacks, the solution based synthesis such as sol-gel, co-precipitation, hydrothermal, microemulsion and auto-combustion techniques have been developed [10]. These approaches enable direct formation of submicron or nanocrystalline $SrFe_{12}O_{19}$ powders without extensive milling. Though they have better control over the particle size and homogeneity, some of these methods require expensive precursors or involve complex time consuming procedures [11-12]. In the pursuit of sustainable and eco-friendly materials, green synthesis strategies have gain importance [13]. The utilization of plant based bio-waste materials such as leaf powder as combustion fuels offer an environmentally benign and cost-effective alternative for nanoparticle production [14]. Therefore, in the present study, Sm doped $SrFe_{12}O_{19}$ were synthesized by auto combustion method using Buteamonosperma leaf as a green fuel. Sm doped $SrFe_{12}O_{19}$ nanoparticles demonstrated effective utilization of sunlight irradiation for catalytic degradation and highlighting their potential in environmental remediation and renewable

energy related applications [15]. Certain synthesized nanoparticles exhibit semiconducting behavior under ultraviolet or solar irradiation due to their suitable band structures, enabling their application in photocatalytic degradation processes. A comparative assessment of photocatalytic performance was conducted for samples containing different samarium percentage [16-17]. In view of the above, in our laboratory the synthesis, characterization, electrochemical application and dye degradation studies have been done [18-19]. In the present work, various percentage of Sm doped $SrFe_{12}O_{19}$ were prepared and the influence of samarium doped nanoparticles on the structure, photocatalytic activity and electrochemical sensing was studied [20-21].

2. MATERIALS AND METHODS

2.1 Materials used

Buteamonosperma (BMS) an indigenous plant species collected from Shivamogga, Karnataka was utilized in this study [22]. Commonly referred to as Palus BMS belongs to the Leguminosae family and is extensively distributed across various regions of India. The leaves of BMS are renowned for containing limo oil which is rich in fatty acids such as oleic, linoleic, lignoceric and palmitic acids. Following collection, the leaves underwent shade drying resulting in a coarse powder that was subsequently stored in an airtight container for subsequent use as showed in Fig.1.Strontium nitrate $Sr(NO_3)_2$, ferric nitrate $Fe(NO_3).9H_2O$ were procured from merck and employed as received without any further purification. Deionized (DI) water was employed throughout the synthesis process.



Fig. 1 Preparation of Butea-monosperma green fuel

2.2 Synthesis

Samarium doped strontium hexaferrites nanoparticles were synthesized using a solution based auto-combustion technique employing BMS as an eco-friendly green fuel Fig.2. Analytical grade strontium nitrate $Sr(NO_3)_2$,ferric nitrate $Fe(NO_3)_3.9H_2O$ and samarium nitrate, $Sm(NO_3)_3.6H_2O$ were accurately measured according to the required stoichiometric ratios [23]. These precursors were dissolved in deionized water under continuous stirring to obtain a clear and homogeneous solution. Finely processed BMS material was then added to the solution functioning as a combustible fuel and as a reducing agent to maintain the appropriate oxidizer fuel balance. The prepared precursor mixture was poured into a heat resistant container and placed inside a furnace preheated to 600 ± 10 °C. Upon heating the solution rapidly evaporated and reached ignition within approximately 15 – 18 seconds triggering a self-propagating combustion reaction [24]. The highly exothermic process caused rapid decomposition of the nitrates accompanied by the release of gaseous byproducts such as N_2O and CO_2. This combustion yielded a voluminous porous and loosely agglomerated powder. The rapid flame front propagation and gas evolution promoted intimate mixing of the reactants shortened diffusion pathways and contributed to the formation of fine particles with relatively narrow size distribution [25]. The synthesized powder was subsequently ground thoroughly to break down soft agglomerates. A small amount of polyvinylpyrrolidone (PVP) binder was added to improve the mechanical strength and compaction behavior of the powder. The mixture was then calcinated at 600 °C for 4 hours to ensure complete phase formation and crystallization. After calcination the powder was pressed into pellets with a diameter of 10 mm and

thickness of approximately 2-3 mm under a pressure of 5-10 kg/cm² for 5 minutes [26]. The compacted pellets were sintered at 1000 °C for 3 hours to enhance densification and grain growth. Finally, the samples were allowed to cool naturally to room temperature inside the furnace resulting in highly crystalline samarium doped $SrFe_{12}O_{19}$ with uniform structural characteristics.



Fig. 2 Schematic representation of synthesis of Sm doped$SrFe_{12}O_{19}$ nanoparticle

2.3 Characterization

The phase purity and crystalline structure of the synthesized Sm doped $SrFe_{12}O_{19}$ nanoparticles (1% and 5% Sm doped $SrFe_{12}O_{19}$) were investigated using a Bruker D8 Advance X-ray diffractometer (XRD) [27]. The vibrational characteristics corresponding to metal-oxygen bonds were analyzed with a Shimadzu FT-IR spectrophotometer (Spirit model serial no A224159). UV-Visible absorption properties and optical band gap of the nanoparticles were examined using a Systronics UV-Vis spectrometer (model 119). Surface morphology of the Sm doped $SrFe_{12}O_{19}$ nanoparticle was studied through scanning electron microscopy (SEM, Zeiss model- EVO LS 15). Further, thestructure and morphological insights were obtained using transmission electron microscopy (TEM) with a Thermo Fisher Talos 200 system.

2.4 Photodegradation activity

The photocatalytic degradation of methylene blue (MB) dye was investigated under sunlight. Key operational parameters studied included initial dye concentration (5-20 ppm) catalyst dosage (5-20 mg) and solution pH ranging from 3 to 11. For each run5 mg of catalyst was dispersed in the dye solution [28]. Prior to illumination the suspension was magnetically stirred in the dark for 30 minutes to establish adsorption-desorption equilibrium between the catalyst surface and the dye molecules. During the photocatalytic process 2mL of aliquots were withdrawn at 30 minutes intervals. The samples were centrifuged to remove catalyst particles and the clear supernatant was analyzed using a UV-Visible spectrophotometer. A decrease in absorbance indicated a reduction in dye concentration. The percentage degradation of MB dye was calculated using the Beer-Lambert law according to equation (1):

$$\% \text{ of Degradation} = \frac{C_i - C_f}{C_i} \times 100 \qquad \text{------- (1)}$$

Where C_i and C_f represents the initial and final concentration of the dye respectively.

3. RESULTS AND DISCUSSION

3.1 X-ray diffraction studies

X-ray diffraction (XRD) patterns of undoped $SrFe_{12}O_{19}$ along with Sm doped $SrFe_{12}O_{19}$ nanoferrites at percentage of 1% and 5% are illustrated in Fig.3. The structural characterization was performed using a Bruker Advance diffractometer (Germany) employing CuKα radiation with a wavelength of 1.5406 Å. All recorded diffraction peaks align well with the standard pattern

of M-type $SrFe_{12}O_{19}$ confirming the presence of a hexagonal crystal structure [29]. Across the samples no prominent impurity peaks are observed indicating that materials are predominantly phase pure. However, upon closer examination of 1% and 5% Sm doped samples a minor secondary phase becomes evident. This addition peak denoted by * indicates the factual formation of a Sm containing secondary phase likely associated with Sm-$SrFe_{12}O_{19}$. The intensity of this peak increases with increasing dopant content [30]. The diffraction peaks with h, k, l values indexed to the planes are (209), (304), (218), (226), (228) (106), (205) and (318) consistent reference data consists with the standard JCPDS card No. 33-1340thereby confirming the retention of the hexagonal systems the interplanar spacing (d_{hkl}) is related to the Miller indices (h, k, l) and lattice parameters (a and c) according to the relation:

$$\frac{1}{d^2hkl} = \frac{4}{3}\left(\frac{h^2 + hk + k^2}{a^2}\right) + \frac{l^2}{c^2}$$

The average crystallite size of the nanoferrites was estimated from the XRD data using the Debye-Scherrer equation:

$$d = \frac{k\lambda}{\beta cos\theta}$$

Where d is the average crystallite size, K (0.89) is the Scherrer's constant in hexagonal symmetry, λ (0.15406 nm) is the wavelength of incident X-rays, θ represents the Bragg's angle and β corresponds to the full width at half maximum (FWHM) of the dominant diffraction peak.

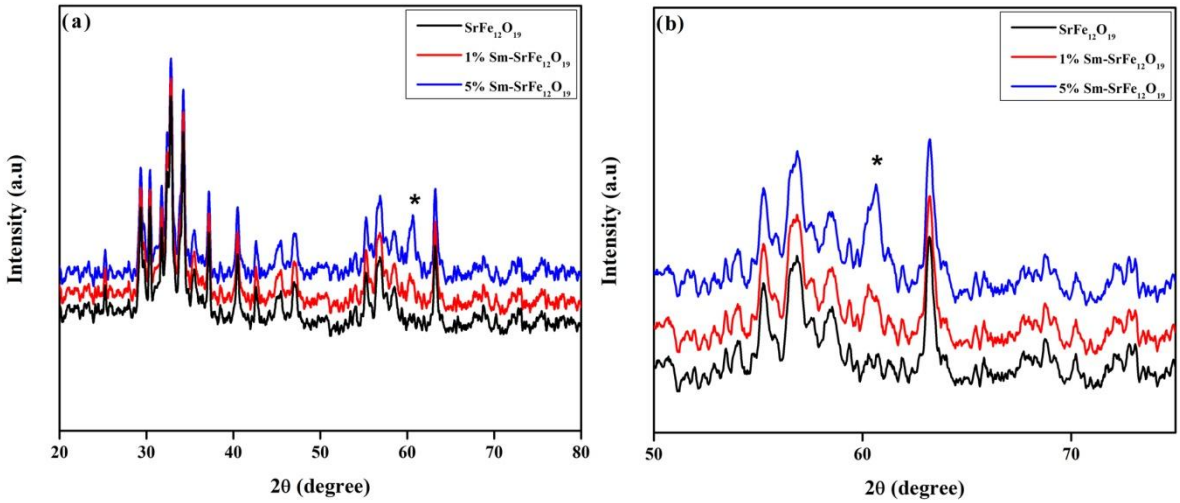

Fig. 3 X-ray diffraction pattern of $SrFe_{12}O_{19}$, 1% and 5% Sm doped $SrFe_{12}O_{19}$ (*the factual formation of a Sm containing secondary phase)

3.2 FTIR Studies

FTIR spectroscopy is an important analytical technique used to investigate structural and chemical modifications occurring during the preparation process particularly during combustion and sintering stages. This technique is useful for identifying the presence of cations in both tetrahedral and octahedral sites of the crystal lattice [31]. It also provides information regarding various crystallographic bonds present in the material. The hygroscopic nature of the synthesized samples can sometimes be indicated by the appearance of very small distortions in the spectra which arise due to moisture absorption from the surrounding environment. The FTIR spectra of Sm doped $SrFe_{12}O_{19}$ with different doping concentration are presented in Fig 4. Two prominent absorption bands are observed at 502 and 587 cm^{-1} which corresponds to the characteristic metal-oxygen stretching vibration associated with the hexagonal lattice structure. Upon incorporation of Sm ions, a slight shift of the peak position toward lower wavenumbers is observed indicating lattice modification while preserving the overall crystal structure of the composition. The band appearing in the range of 400-1000 cm^{-1} particularly the peak at 502 cm^{-1} is attributed to the low frequency band associated with the Fe-O stretching vibrations at the octahedral sites. In contrast, the band at 587 cm^{-1} corresponds to the higher frequency band related to the Fe-O vibrations at the tetrahedral sites [32]. These characteristic bands provide important information regarding the formation and structural arrangement of hexaferrites. The vibrational

frequency at the tetrahedral site is generally higher than that at the octahedral site due to difference in bond length and bonding environment within the crystal lattice. According to Hooke's law the vibrational frequency of a bond depends on the mass of the atoms and the bond strength where heavier atoms require greater vibrational energy.

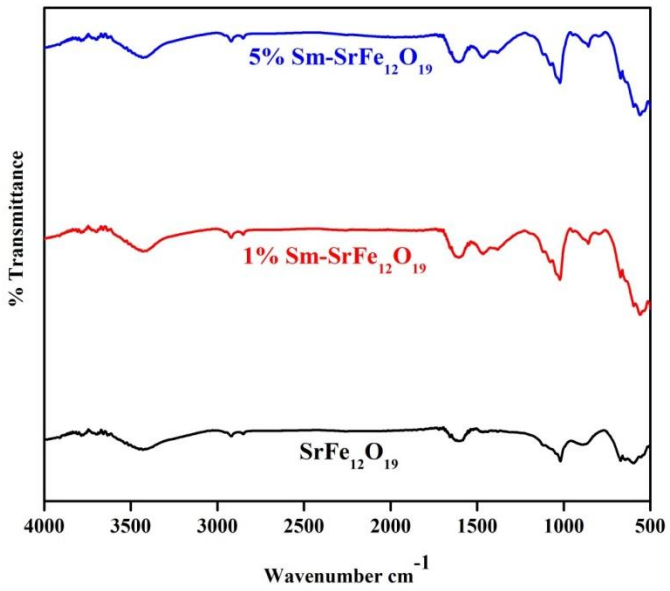

Fig. 4 FTIR spectra of $SrFe_{12}O_{19}$, 1% Sm and 5% Sm doped $SrFe_{12}O_{19}$

3.3 UV-Vis spectroscopic studies

UV-Visible absorption spectra were recorded in the wavelength range of 200-800 nm as presented in Fig.5. All prepared samples including pristine $SrFe_{12}O_{19}$ and Sm doped $SrFe_{12}O_{19}$nanoparticles exhibited pronounced absorption bands in the 350-400 nm. This regionfalls within the visible spectrum, indicating that the synthesized materials possess the capability to effectively absorb visible light [33].The $SrFe_{12}O_{19}$nanoparticles in Fig.5 displayed a well-defined absorption peak at 362 nm, corresponding to estimated band gap energy of 3.44 eV. In contrast, the 1% Sm doped $SrFe_{12}O_{19}$ exhibit an intense absorption peak at 366 nm which corresponds to the higher band gap value 3.38 eV. Similarly, the 5% Sm doped $SrFe_{12}O_{19}$ nanoparticles exhibited a characteristic absorption peak at 370 nm associated with a band gap energy of 3.35eV.A comparative evaluation of the band gap energies reveals a noticeable variation among the samples. However, the 5% Sm doped $SrFe_{12}O_{19}$ demonstrates a reduced band gap relative to the 1% doped sample. This reduction in the band gap is advantageous for further characterization and photocatalytic application as it facilitates enhanced light absorption and improved charge carrier activity. Consequently, the 5% Sm doped sample exhibits superior photocatalytic performance in dye degradation when compared to both the undoped and 1% doped counterparts. Based on these results, the composition was selected for further detailed characterization and application studies. The optical band gap was determined using the Kubelka-Munk function a widely accepted method for diffuse reflectance data analysis as expressed in the equation (3).

$$[F(R)\ h\nu]^n = A\ (h\nu) - E_g \qquad \text{---------- (2)}$$

$$F(R) = \frac{(1-R)^2}{2R} \qquad \text{---------- (3)}$$

Where, R is the reflectance; A is the proportionality constant related to the transition probability; h is Plank's constant; v is the frequency of the incident radiation and n is an exponent that depends on the nature of the electronic transition.

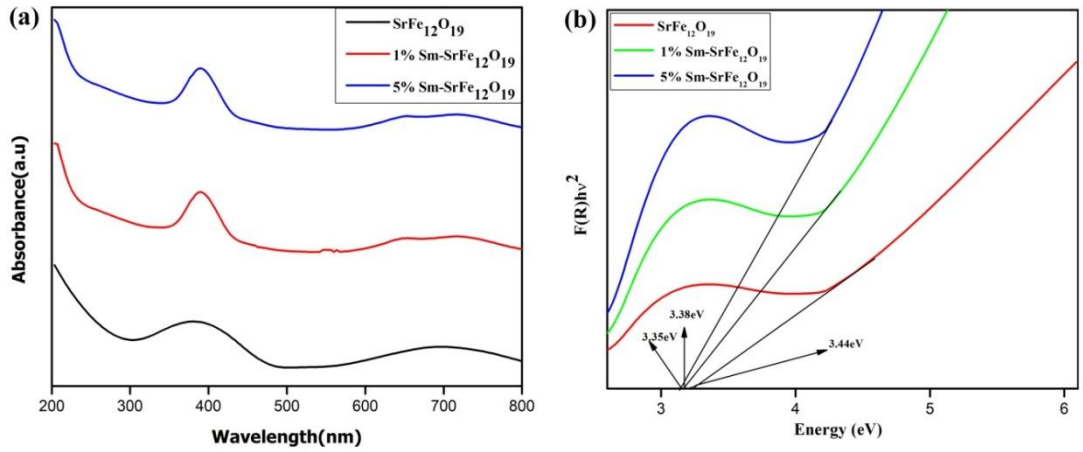

Fig. 5 (a) UV-Vis absorbance spectra of $SrFe_{12}O_{19}$, 1% Sm and 5% Sm doped $SrFe_{12}O_{19}$, (b) Bandgap energy of $SrFe_{12}O_{19}$, 1% Sm and 5% Sm doped $SrFe_{12}O_{19}$.

3.4 SEM

Field emission scanning electron microscopy (FE-SEM) image shown in Fig.6 illustratethe surface morphology of the 5% Sm doped $SrFe_{12}O_{19}$samples. In general, the micrographs reveal the formation of distinct well aligned hexagonal plate like grains with clear faceting. However, this characteristic morphology appears less pronounced in the sample containing low percentage of Sm [34]. A systematic decrease in the average particle size is observed as the dopant concentration increases suggesting that the incorporation of Sm ions suppresses the grain growth during the synthesis process. In addition,comparison of the crystallite size obtained from Rietveld refinement with the particle size estimated from FE-SEM analysis conclude that each observed particle consists of several smaller crystallites aggregated together.

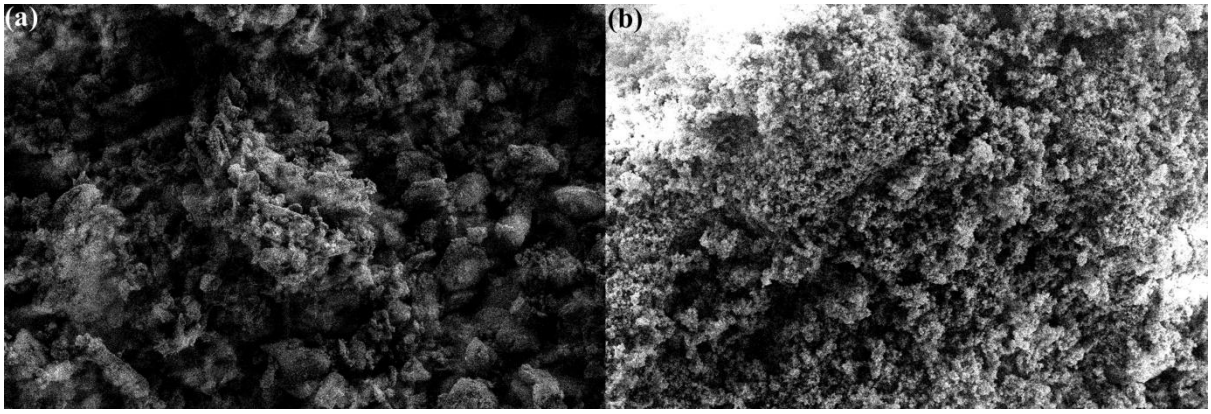

Fig. 6 (a-b) SEM image of 5% Sm doped $SrFe_{12}O_{19}$

3.5 EDX

Energy dispersive X-ray (EDX) analysis was carried out using a Carl Zeiss EVOLS15 instrument (Germany) to investigate the elemental composition of the synthesized Sm doped $SrFe_{12}O_{19}$nanoparticles as showed in Fig.7. This EDX analysis was performed to confirm the incorporation of Sm as a dopant and to evaluate the elemental composition of the prepared samples [35]. The spectrum clearly reveals the presence of strontium, iron, samarium and oxygen verifying the successful inclusion of Sm in the material. Furthermore, the EDX results support the exultant formation of the desired nanoparticles. The appearance of well-defined peaks indicates good crystallinity of the synthesized particles. While, the absence of any unexpected peaks suggests that the samples are free from impurities confirming that no contamination occurred during the synthesis process.

Natural Resources for Human Health
eISSN: 2583-1194

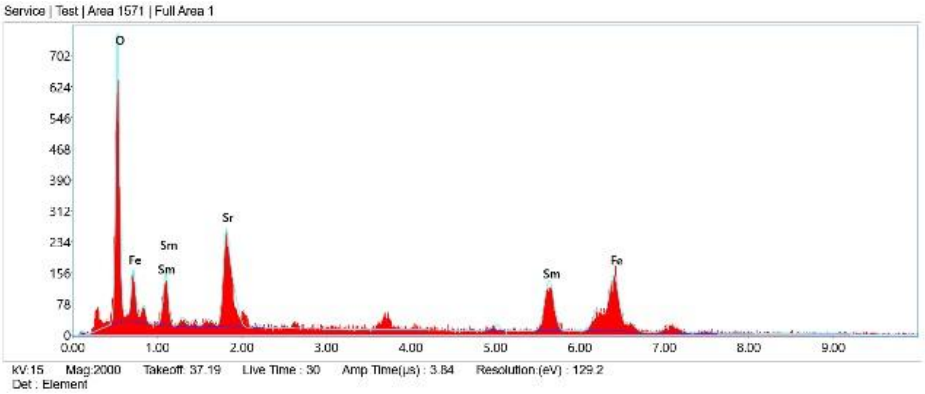

Fig. 7 Elemental mapping and energy dispersive X-ray (EDX) spectrum of 5% Sm doped $SrFe_{12}O_{19}$.

3.6 TEM

To investigate the morphological and structural characteristics the synthesized 5% Sm doped $SrFe_{12}O_{19}$ nanoparticles were analyzed using transmission electron microscopy (TEM) Fig.8(a). The TEM images reveal that the nanoparticles exhibit irregular shapes are densely packed and display good uniformity throughout the sample. Particle size distribution was evaluated using a histogram [36]. The average particle size was found to be approximately 37.90nm Fig. 8(e) which is in close agreement with the values obtained from X-ray diffraction thereby confirming the successful formation of nanoparticles. High-resolution TEM (HR-TEM) analysis was performed to further examine the morphology, crystallinity and size distribution of the nanoparticles. The HR-TEM images Fig. 8(b) indicate a predominantly hexagonal morphology with a slight tendency toward agglomeration. The particle size range supporting the nanocrystalline nature of the synthesized material [37]. The observed variation in particle size can be attributed to particle agglomeration. The HR-TEM images also display well-resolved lattice fringes with an interplanar spacing (d-spacing) of approximately 0.271 nm Fig. 8(c). This value corresponds to the (106) crystallographic plane confirming the crystalline structure of the 5% Sm doped $SrFe_{12}O_{19}$ nanoparticles. The clear lattice fringes further indicate the high crystallinity of the sample. Selected area electron diffraction (SAED) patterns provide additional insight into the crystalline structure and orientation [38]. As illustrated inFig.8(d)the SAED pattern shows distinct diffraction rings corresponding to the (106), (209), (220), (406) and (002) planes. The presence of these rings along with spot like features suggests a well ordered atomic arrangement and high crystallinity. In addition the observed diffraction patterns reflect the expected hexagonal symmetry of the ferrite structure confirming the underlying crystal lattice and phase purity of the material.

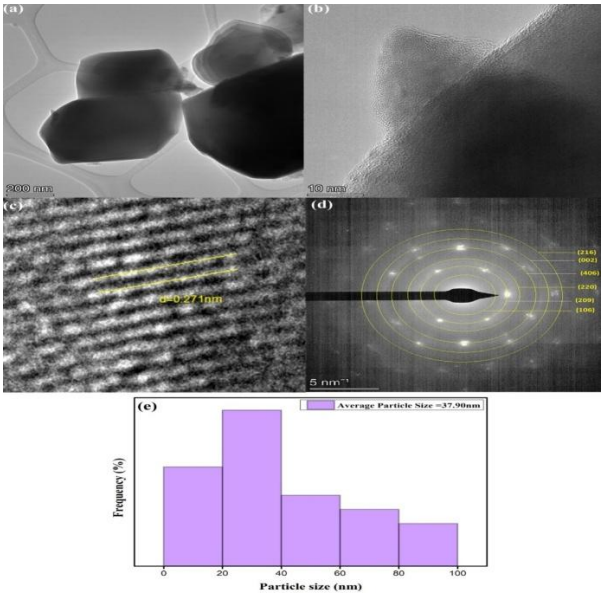

Fig. 8 (a)TEM (b) HR-TEM (c) d-spacing (d) SAED pattern image (e) Average particle size of 5% Sm doped $SrFe_{12}O_{19}$

Natural Resources for Human Health
eISSN: 2583-1194

4 PHOTODEGRADATION STUDIES

4.1 Mechanism of Photodegradation of organic dyes

Photodegradation of organic dyes begins when light energy is absorbed by a photocatalyst dye system [39]. Upon irradiation, photons provide sufficient energy to excite electrons from the valance band to the conduction band of the photocatalyst generating electron hole pairsFig.9. The excited electron in the conduction band and the corresponding holes in the valence band play a crucial role in initiating surface redox reactions. The photogenerated electrons interact with adsorbed oxygen molecules leading to the formation of superoxide radical anions ($\cdot O_2^-$). Simultaneously, the holes react with water molecules or hydroxide ions to produce highly reactive ($\cdot OH$). These reactive oxygen species are strong oxidizing agents that attack functional groups present in dye molecules particularly those containing sulfur and nitrogen [40]. Through, a series of oxidative reactions these radicals progressively break down complex dye structure such as methylene blue into simpler and less harmful compounds. As the degradation process continues the dye molecules are ultimately mineralized into environmentally benign products thereby reducing their ecological impact. This mechanism highlights the effectiveness of photocatalysis in converting light energy into chemical processes that facilitate the degradation of hazardous organic pollutants.

$SmSrFe_{12}O_{19} + h\nu\ (vis) \rightarrow SmSrFe_{12}O_{19}\ (e^-CB + h^+VB)$

$SmSrFe_{12}O_{19}\ (e\text{-}CB) + O_2 \rightarrow O_2\cdot$

$O_2\cdot + h^+ \leftrightarrow HOO\cdot$

$2HOO\cdot \rightarrow H_2O_2 + O_2$

$SmSrFe_{12}O_{19}\ (h^+VB) + H_2O \rightarrow HO\cdot + H^+$

$Dye + HO\cdot + O_2\cdot \rightarrow CO_2 + H_2O\ (Byproduct)$

$Dye + SmSrFe_{12}O_{19}(h^+VB) \rightarrow Oxidation\ Product$

$Dye + SmSrFe_{12}O_{19}\ (e^-CB) \rightarrow Reduction\ Product$

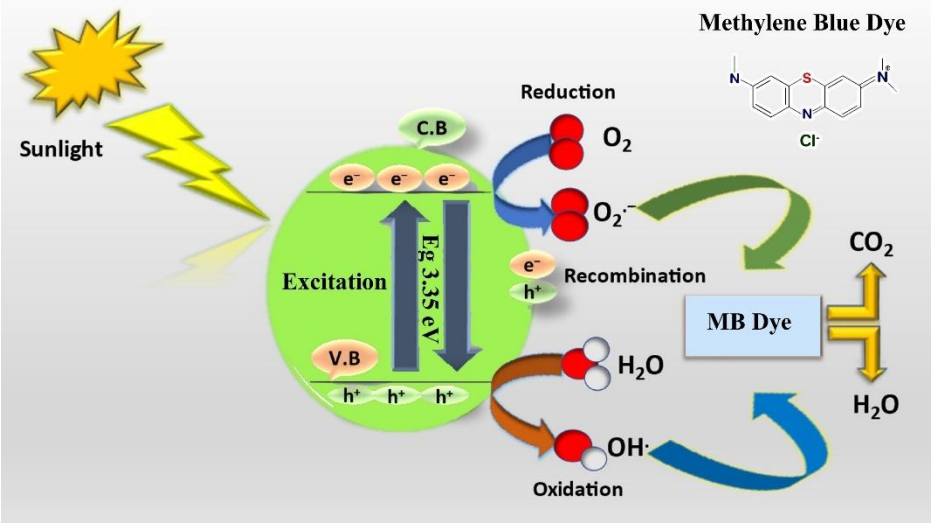

Fig. 9 Proposed mechanism for photodegradation of MB dye by 5% Sm doped $SrFe_{12}O_{19}$ under sunlight.

4.2 Comparative Degradation Study

The photocatalytic performance of Sm doped $SrFe_{12}O_{19}$ nanoparticles was systematically evaluated for the degradation of two representative dyes i.e an anionic dye methyl orange (MO) and a cationic dye methylene blue (MB). The results reveal a clear dependence of degradation efficiency on the nature of the dye [41]. As illustrated in Fig.10(a) the Sm doped $SrFe_{12}O_{19}$ nanoparticles exhibited significantly higher activity towards the cationic MB dye achieving a degradation efficiency of approximately 84%. In contrast, the anionic MO dye showed comparatively lower degradation with an efficiency of around

48% under similar conditions. This variation can be attributed to the physicochemical properties of the photocatalyst particularly its surface charge characteristics and electronic structure. The surface of Sm doped $SrFe_{12}O_{19}$ NPs is predominantly composed of oxygen atoms leading to a negatively charged surface environment due to electron rich regions. This negatively charged surface promotes stronger electrostatic attraction with cationic dye molecules such as MB enhancing adsorption and facilitating more efficient photocatalytic degradation. Conversely, the interaction with anionic dyes like MO is less favorable due to electrostatic repulsion resulting in reduced degradation efficiency. Further investigationconfirms the MB degradation by 5% Sm doped $SrFe_{12}O_{19}$NPs and 1%Sm doped $SrFe_{12}O_{19}$ nanoparticles exceeded 82% and 64% respectively owing to enhanced adsorption and subsequent photocatalytic reaction on the nanoparticle surface. In comparison MO degradation remained relatively low at approximately 55-65% as represented in Fig. 10 (b). These findings highlight the critical role of dye catalyst interactions governed by charge compatibility and surface morphology. Based on these results subsequent studies were focused on MB as the model pollutant due to its significantly higher degradation efficiency. Among the different composition examined, 5%Sm doped $SrFe_{12}O_{19}$ nanoparticles demonstrated the optimal performance and achieving the highest degradation efficiency as shown in Fig. 10(c). This optimized composition was therefore selected for detailed mechanistic studies and further photocatalytic investigation.

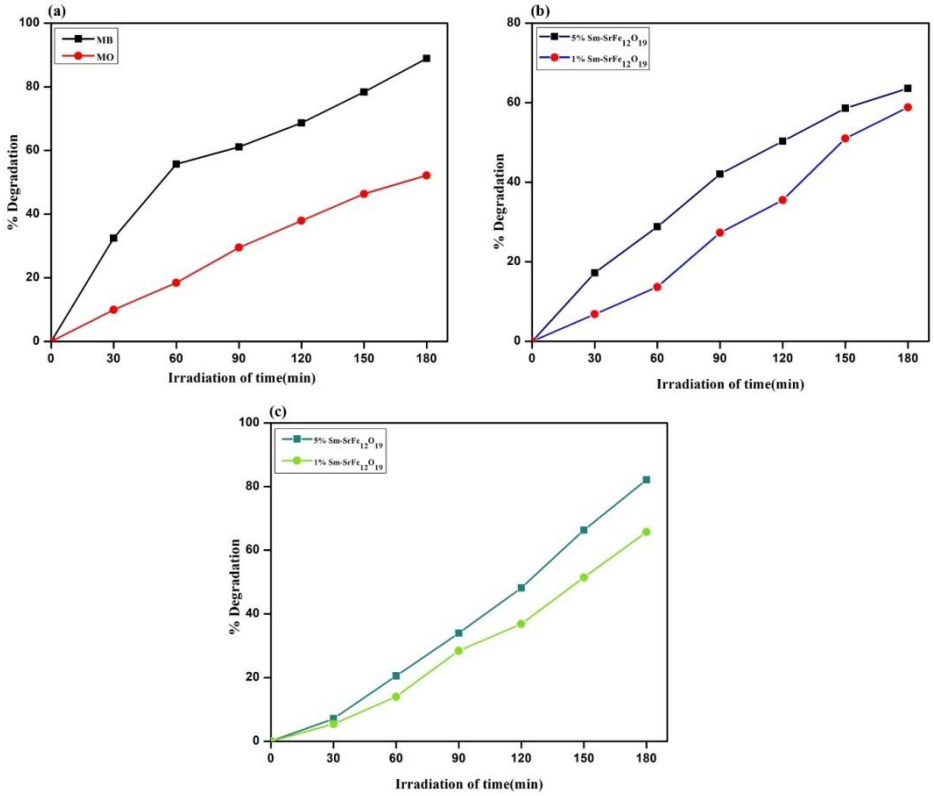

Fig. 10 (a) Percentage degradation of MB and MO dye using $SrFe_{12}O_{19}$. (b) Percentage degradation of MO dye using 1% and 5%$SrFe_{12}O_{19}$, (c) Percentage degradationof MB dye using 1% and 5% $SrFe_{12}O_{19}$.

4.3 Effect of dye concentration

The influence of dye concentration on the photodegradation efficiency of MB was systematically investigated using a fixed amount 5 mg of $SrFe_{12}O_{19}$NPshave been compared in Fig. 11(a) and 5 mg of 5% Sm-$SrFe_{12}O_{19}$ NPs Fig. 11(b) under neutral pH condition [42]. The experimental results presented in Fig.11were obtained by varying the initial dye concentration from 5 to 20 ppm. A clear decline in degradation efficiency was observed with increasing dye concentration. This reduction in efficiency can be attributed primarily to the limited penetrating of UV light in more concentrated dye solutions. At higher concentration, the solution becomes increasingly opaque restricting the transmission of light to the catalyst surface. As a result, the generation and effective separation of photogenerated electron-hole pairs are significantly hindered thereby supporting the overall photocatalytic activity. To further elucidate this effect, an additional experiment were conducted with lower dye concentrations ranging from 5 to 20 ppm while maintaining the same catalyst loading and maintaining the same

experimental conditions as shown in Fig.11. The highest degradation efficiency was achieved at an optimal concentration of 5 ppm. Beyond this concentration a progressive decrease inphotocatalytic performance was again observed. The inverse relationship between dye concentration and degradation efficiency highlights the critical role of light availability in photocatalytic processes. At elevated concentrations the reduced light penetration limits catalyst activation and diminishes electron-hole separation efficiency ultimately lowering the degradation rate of MB [43]. These findings emphasize the importance of optimizing dye concentration to maximize photocatalytic performance. Proper control of this parameter is essential for enhancing the efficiency of dye degradation and improving the practical applicability of Sm-$SrFe_{12}O_{19}$NPs.

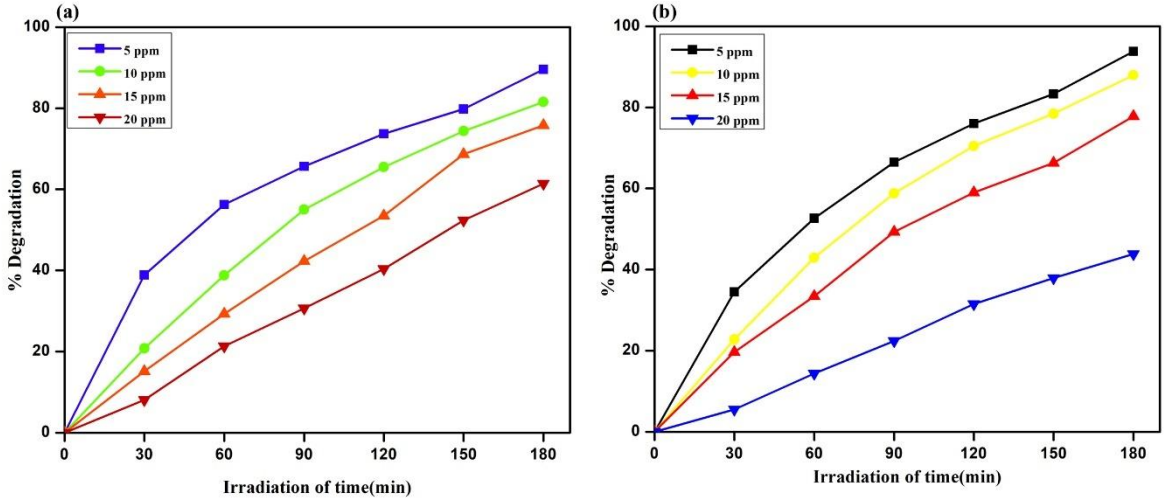

Fig. 11 (a) Effect of dye concentration of $SrFe_{12}O_{19}$, (b) Effect of dye concentration 5% Sm-$SrFe_{12}O_{19}$,

4.4 Effect of Catalyst Concentration

The influence of catalyst loading on the photocatalytic degradation efficiency (PDE) of MB was systematically investigated by varying the amount of $SrFe_{12}O_{19}$ nanoparticles indicated in Fig.12(a) and 5% Sm-$SrFe_{12}O_{19}$ nanoparticles Fig.12(b). Different catalyst dosages (5, 10, 15, 20 mg) were dispersed in 100 mL of dye solution with an initial concentration of 5 ppm and the corresponding results are presented in Fig.12. The experimental findings indicate that increasing the catalyst concentration enhances the degradation efficiency of MB upto an optimum level [44]. This improvement can be attributed of active surface sites with higher catalyst loading which facilitates increased adsorption of dye molecules and promotes photocatalytic reactions. The enhanced surface activity leads to the generation of a larger number of photogenerated charge carriers (electron-hole pairs) resulting in the formation of reactive species such as hydroxyl radicals (·OH) and superoxide radicals ($\cdot O_2^-$). These species play a key role in the oxidative degradation of MB molecules. However, beyond an optimal catalyst dosage the improvement in degradation efficiency becomes less significant. Among the studied concentration 5 mg of catalyst exhibited the highest photocatalytic performance indicating that it provides an optimal balance between surface area availability and effective light utilization. Excessive catalyst loading may lead to light scattering and reduced photon penetration thereby limiting the overall efficiency of the system. In order to further validate this trend further, the addition experiments were conducted using catalyst loadings ranging from 5 to 20 mg in 100 mL of dye solution under UV irradiation. The results confirm that although increasing catalyst weight generally enhance degradation due to the availability of more active sites the optimal performance is consistently achieved at 5 mg. At this concentration sufficient active sites are available to maximize the generation of reactive species without compromising light absorption [45]. Overall, these results highlight the critical role of catalyst dosage in optimizing photocatalytic performance. The selection of an appropriate catalyst concentration such as 5 mg in this study ensures efficient utilization of active sites and maximizes the degradation rate of MB.

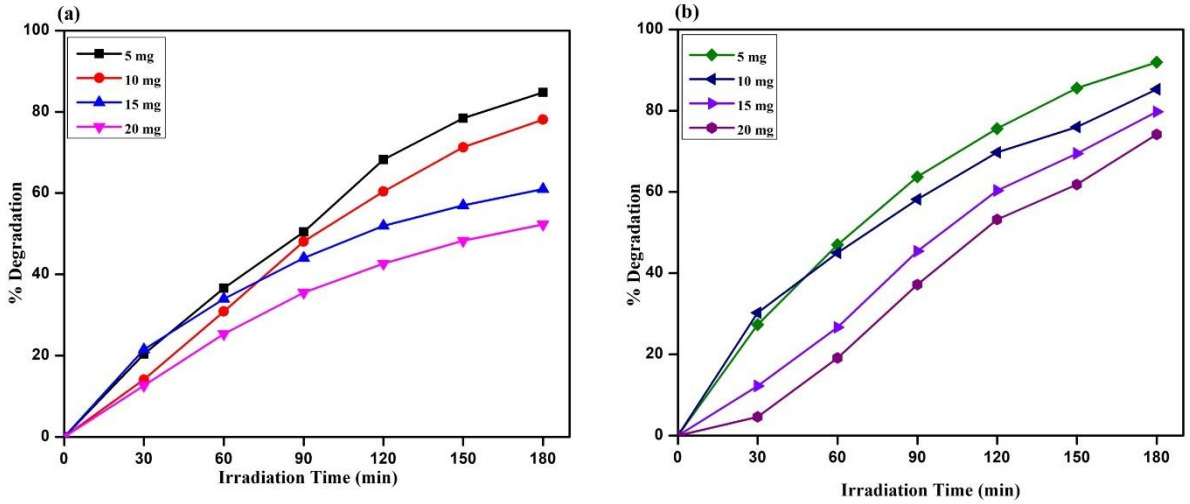

Fig. 12 (a) Effect of catalytic load of $SrFe_{12}O_{19}$, (b) Effect of catalytic load of 5% Sm-$SrFe_{12}O_{19}$.

4.5 Effect of pH

The effect of solution pH on the photocatalytic degradation of MB was studied over a pH range from 3 to 11 using 5 mg of Sm-$SrFe_{12}O_{19}$ and with an initial dye concentration of 5 ppm. The corresponding results are presented inFig 13(a and b). The experimental data clearly indicate that the degradation efficiency increases with increasing pH [46]. At an acidic pH of 3, the photocatalytic degradation efficiency was approximately 65-70%. When the pH was 5, the efficiency improved to around 68-75%. A further rise in pH resulted in continued enhancement of degradation performance with maximum efficiencies of 78-85% achieved under strongly alkaline conditions (pH 11). This improvement in photocatalytic activity at higher pH values can be attributed to the surface charge properties of the Sm-$SrFe_{12}O_{19}$. Under alkaline conditions, the catalyst surface becomes more negatively charged which enhances the electrostatic attraction between the photocatalyst and the positively charged MB molecules. This increased adsorption facilitates more efficient interaction between the dye molecules and reactive species generated on the catalyst surface. Moreover, alkaline conditions favour the generation of hydroxyl radicals (·OH) due to the higher availability of hydroxide ions further promoting the oxidative degradation of MB. The combined effect of enhanced radical formation leads to superior photocatalytic performance at elevated pH levels [47]. Overall, these findings demonstrate that the pH is a critical parameter influencing photocatalytic efficiency. Optimizing the solution pH particularly toward alkaline conditions significantly enhances the degradation of MB and improves the overall effectiveness of the photocatalytic treatment process.

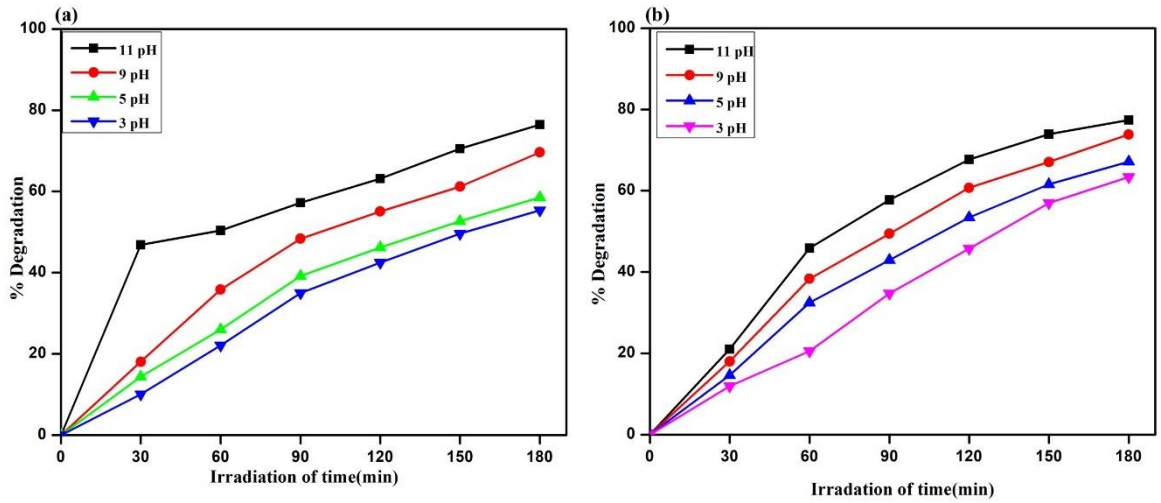

Fig. 13 (a) Effect of different pH of $SrFe_{12}O_{19}$, (b) Effect of different pH of 5% Sm-$SrFe_{12}O_{19}$.

Natural Resources for Human Health
eISSN: 2583-1194

4.6 Effect of Scavengers

To elucidate the degradation mechanism and identify the key reactive species involved in the photocatalytic process, scavenger studies were performed using specific quenching agents [48]. The selected scavengers included tert-butyl alcohol (TBA, 1mM) for hydroxyl radicals (·OH), potassium dichromate ($K_2Cr_2O_7$, 1mM) for electrons ascorbic acid (1mM) for superoxide radicals ($\cdot O_2^-$) and ethylenediaminetetraacetic acid (EDTA, 1mM) for photogenerated holes (h^+) and the results are presented in Fig 14. The introduction of EDTA resulted in only a slight decrease in the degradation efficiency of MB suggesting that photogenerated electrons play a relatively minor role in the overall degradation process. In contrast, the addition of TBA significantly suppressed the photocatalytic activity indicating that hydroxyl radical are major contributors to the degradation mechanism. Similarly the presence of $K_2Cr_2O_7$ led to a pronounced reduction in degradation efficiency highlighting the importance of charge carrier dynamics in the process. Further, the use of ascorbic acid also affected the degradation performance confirming the participation of superoxide radicals in the reaction pathway. Overall, the marked inhibition observed in the presence of TBA and hole scavengers demonstrated that hydroxyl radicals (·OH) and photogenerated holes (h^+) are the dominant reactive species governing the photocatalytic degradation of MB. These findings provide clear evidence that the degradation process is primarily driven by oxidative pathways involving ·OH radicals and holes with secondary contributions from other reactive oxygen species. The scavengers study thus offers valuable insight into the mechanistic aspects of photocatalytic degradation and highlights the critical role of reactive intermediates in enhancing the efficiency of the system.

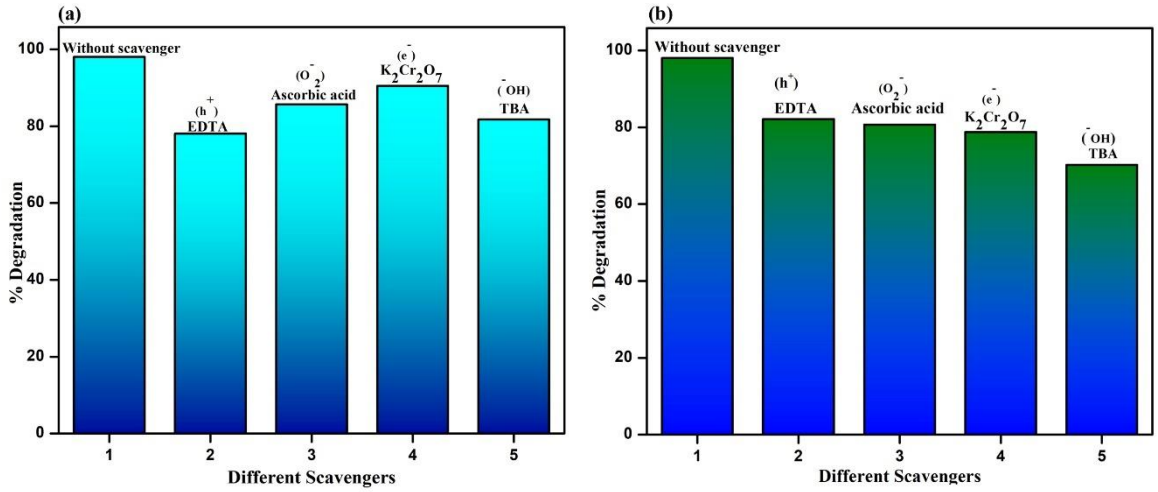

Fig. 14 (a) Effect of different scavengers on the degradation of MB dye using $SrFe_{12}O_{19}$, (b) Effect of different scavengers on the degradation of MB dye using 5% Sm-$SrFe_{12}O_{19}$.

4. CONCLUSION

This study reports the successful synthesis of samarium doped $SrFe_{12}O_{19}$ using an environmentally sustainable green synthesis method. BMS leaf powder was utilized as a green fuel during the combustion process serving both as a carbon source and a reducing agent during calcination. Among various synthesis methods the combustion technique employed offers distinct advantages including operational simplicity, rapid processing, high yield and the ability to produce homogeneous materials. The prepared nanoparticles were systematically characterized using XRD, SEM, FT-IR, EDS etc., Compared to undoped $SrFe_{12}O_{19}$, the doped nanoparticles exhibited significantly improved photocatalytic activity. The results highlight the potential of samarium doped $SrFe_{12}O_{19}$ for environmental remediation application particularly in the treatment of organic contamination in water. Their improved catalytic efficiency and stability make them suitable for long term use in photocatalytic systems.

ACKNOWLEDGEMENTS

Authors are thanking to VGST govt of Karnataka, India for providing IR, UV spectroscopy facilities and Sahyadri Science College, Shivamogga-577203, for providing laboratory facilities.

CONFLICT OF INTEREST

The authors declare that there is no conflict of interest.

DATA AVAILABILITY STATEMENT

Data supporting the findings of this study are available from the corresponding author upon reasonable request.

REFERENCES

[1] Khan, Salman Naeem, Amna Mir, Saima Manzoor, and Rafia Raees. "Effect of rare earth doping on the electromagnetic response of hard ferrites SrFe12O19 for potential application in high-frequency devices." Materials Chemistry and Physics 320 (2024): 129378.

[2] Wang, Siyuan, Jingwu Zheng, Wei Cai, Liang Qiao, Yao Ying, Haibo Chen, Wangchang Li, Jing Yu, Juan Li, and Shenglei Che. "High coercivity in Sm-doped SrFe12O19 powders with spherical morphology prepared by ultrasonic spray pyrolysis." Ceramics International 50, no. 6 (2024): 9510-9519.

[3] Thippeswamy, A., Prabhakar Chavan, and G. Krishnamurthy. "magnetic and photocatalytic properties of samarium doped strontium hexaferrites synthesized by auto-combustion method." Rasayan J.Chem 18, no.3 (2025): 1305-1315.

[4] Faraz, Mohd, Faria K. Naqvi, Mohammad Shakir, and Neeraj Khare. "Synthesis of samarium-doped zinc oxide nanoparticles with improved photocatalytic performance and recyclability under visible light irradiation." New Journal of Chemistry. 42 (3) (2018) 2295-2305.

[5] Dakhel, A. A. "Transparent conducting properties of samarium-doped CdO." Journal of Alloys and Compounds. 475 (1-2) (2009) 51-54.

[6] Chand, Prakash, and Vishal Singh. "Enhanced visible-light photocatalytic activity of samarium-doped zinc oxide nanostructures." Journal of Rare Earths 38 (1) (2020) 29-38.

[7] Lakshmikantha, J., G. Krishnamurthy, B. M. Nagabhushan, C. S. Naveen, and E. Melagiriyappa. "Effect of ce3+ substitution on sr2+; structural and magnetic properties of nanocrystalline SRFE12O19 hexaferrites prepared by self-propagation method using mixed fuels." Journal of Superconductivity and Novel Magnetism 35, no. 9 (2022): 2485-2492.

[8] Abbas, Yasir, and M. Anis-ur-Rehman. "Structural, dielectric and transport properties of samarium-doped cobaltites." Ceramics International. 48 (8) (2022) 10638-10649.

[9] Hu, Lanying, Hongwei Song, Guohui Pan, Bin Yan, Ruifei Qin, Qilin Dai, Libo Fan, Suwen Li, and Xue Bai. "Photoluminescence properties of samarium-doped TiO2 semiconductor nanocrystalline powders." Journal of Luminescence. 127 (2) (2007) 371-376.

[10] Nalwa, K. S., A. Garg, and A. Upadhyaya. "Effect of samarium doping on the properties of solid-state synthesized multiferroic bismuth ferrite." Materials Letters 62 (6-7) (2008) 878-881.

[11] Chen, Pu, Fen Wang, Yinpo Qiao, and Zhen Zhang. "Luminescence of samarium doped hydroxyapatite containing strontium: Effects of doping concentration." Journal of Rare Earths. 40 (3) (2022) 398-405.

[12] Sun, Rui, Po Lu, Donglei Zhou, Wen Xu, Nan Ding, He Shao, Yu Zhang et al. "Samarium-doped metal halide perovskite nanocrystals for single-component electroluminescent white light-emitting diodes." ACS Energy Letters. 5 (7) (2020) 2131-2139.

[13] Eraiah, B. "Optical properties of samarium doped zinc-tellurite glasses." Bulletin of Materials Science. 29 (4) (2006) 375-378.

[14] Anthonyraj, C., M. Muneeswaran, S. Gokul Raj, N. V. Giridharan, V. Sivakumar, and G. Senguttuvan. "Effect of samarium doping on the structural, optical and magnetic properties of sol–gel processed BiFeO3 thin films." Journal of Materials Science: Materials in Electronics. 26 (1) (2015) 49-58.

[15] Jebathew, A. Jesu, M. Karunakaran, Mohd Shkir, H. Algarni, S. AlFaify, Aslam Khan, Najla Alotaibi, and Thamraa Alshahrani. "High sensitive samarium-doped ZnS thin films for photo-detector applications." Optical Materials. 122 (2021) 111649.

[16] Lakshmikantha, J., G. Krishnamurthy, R. Hanumantha Nayak, Malathesh Pari, N. Ranjitha, and Nagaraj Naik. "Synthesis, structure, thermal, magnetic, dielectric properties of Ce3+ doped M-type SrFe12O19 and electrochemical determination of L-cysteine." Inorganic Chemistry Communications 146 (2022): 110175.

[17] Morais, Diana Santos, Joao Coelho, Maria Pia Ferraz, Pedro Sousa Gomes, Maria Helena Fernandes, Nandyala Sooraj Hussain, José Domingos Santos, and Maria Ascensão Lopes. "Samarium doped glass-reinforced hydroxyapatite with

enhanced osteoblastic performance and antibacterial properties for bone tissue regeneration." Journal of Materials Chemistry B. 2 (35) (2014) 5872-5881.

[18] Kumar, D. Ranjith, K. S. Ranjith, and RT Rajendra Kumar. "Structural, optical, photocurrent and solar driven photocatalytic properties of vertically aligned samarium doped ZnO nanorod arrays." Optik. 154 (2018) 115-125.

[19] Kumar, D. Ranjith, K. S. Ranjith, L. R. Nivedita, and RT Rajendra Kumar. "Effect of samarium doping on structural, optical and magnetic properties of vertically aligned ZnO nanorod arrays." Journal of Rare Earths. 35 (10) (2017): 1002-1007.

[20] Rhaman, M. M., M. A. Matin, M. A. Hakim, and M. F. Islam. "Dielectric, ferroelectric and ferromagnetic properties of samarium doped multiferroic bismuth ferrite." Materials Research Express. 6 (12) (2019) 125080.

[21] Wang, Sea-Fue, Chun-Ting Yeh, Yuh-Ruey Wang, and Yu-Chuan Wu. "Characterization of samarium-doped ceria powders prepared by hydrothermal synthesis for use in solid state oxide fuel cells." Journal of Materials Research and Technology 2 (2) (2013): 141-148.

[22] MV, Naveen, T. L. Soundarya, Y. T. Ravikiran, and G. Nagaraju. "Facile Green Synthesis of Ni/Nio/Moo3 Nanocomposite for Photocatalytic, Chromium (Vi) Reduction, Electrochemical Dopamine (Da) and Humidity Sensor Application." G, Facile Green Synthesis of Ni/Nio/Moo3 Nanocomposite for Photocatalytic, Chromium (Vi) Reduction, Electrochemical Dopamine (Da) and Humidity Sensor Application.

[23] Tuomela, Anu, Meng Zhang, Marko Huttula, Simas Sakirzanovas, Aivaras Kareiva, Anatoli I. Popov, Anna P. Kozlova, S. Assa Aravindh, Wei Cao, and Vladimir Pankratov. "Luminescence and vacuum ultraviolet excitation spectroscopy of samarium doped SrB4O7." Journal of Alloys and Compounds 826 (2020) 154205.

[24] Li, Haiyan. "Investigation of the structural, magnetic, impedance properties in samarium-doped yttrium iron garnet." Ceramics International. 46 (10) (2020): 15408-15416.

[25] Kundu, Subrata, Narottam Sutradhar, R. Thangamuthu, B. Subramanian, Asit Baran Panda, and M. Jayachandran. "Fabrication of catalytically active nanocrystalline samarium (Sm)-doped cerium oxide (CeO2) thin films using electron beam evaporation." Journal of Nanoparticle Research. 14 (8) (2012) 1040.

[26] Meng, Xudong, Bing Han, Yanfeng Wang, and Jingyu Nan. "Effects of samarium doping on the electrochemical performance of LiFePO4/C cathode material for lithium-ion batteries." Ceramics International. 42 (2) (2016) 2599-2604.

[27] Koettgen, Julius, Tobias Zacherle, Steffen Grieshammer, and Manfred Martin. "Ab initio calculation of the attempt frequency of oxygen diffusion in pure and samarium doped ceria." Physical Chemistry Chemical Physics. 19 (15) (2017) 9957-9973.

[28] Wattanathana, Worawat, Chatchai Veranitisagul, Suttipong Wannapaiboon, Wantana Klysubun, Nattamon Koonsaeng, and Apirat Laobuthee. "Samarium doped ceria (SDC) synthesized by a metal triethanolamine complex decomposition method: Characterization and an ionic conductivity study." Ceramics International. 43 (13) (2017): 9823-9830.

[29] Elisa, M., B. A. Sava, I. C. Vasiliu, R. C. C. Monteiro, J. P. Veiga, L. Ghervase, I. Feraru, and R. Iordanescu. "Optical and structural characterization of samarium and europium-doped phosphate glasses." Journal of Non-Crystalline Solids. 369 (2013) 55-60.

[30] Di, Jing, Mingming Chen, Chengyang Wang, Jiaming Zheng, Liangdong Fan, and Bin Zhu. "Samarium doped ceria–(Li/Na) 2CO3 composite electrolyte and its electrochemical properties in low temperature solid oxide fuel cell." Journal of Power Sources. 195 (15) (2010): 4695-4699.

[31] Kalyk, Fariza, Algita Stankevičiūtė, Gintarė Budrytė, Giedrė Gaidamavičienė, Artūras Žalga, Rita Kriūkienė, Žydrūnas Kavaliauskas, Marzena Leszczyńska, and Brigita Abakevičienė. "Comparative study of samarium-doped ceria nanopowders synthesized by various chemical synthesis routes." Ceramics International. 46 (15) (2020): 24385-24394.

[32] Patil, Jyoti V., Sawanta S. Mali, and Chang Kook Hong. "Boosting the stability of fully-inorganic perovskite solar cells through samarium doped CsPbI2Br perovskite." ACS Sustainable Chemistry & Engineering. 8 (43) (2020) 16364-16371.

[33] Pratibha, S., B. Chethan, Y. T. Ravikiran, N. Dhananjaya, and V. Jagadeesh Angadi. "Enhanced humidity sensing performance of Samarium doped Lanthanum Aluminate at room temperature." Sensors and Actuators A: Physical. 304 (2020) 111903.

[34] Tang, Xuyao, Zimeng Hu, Vladimir Koval, Bin Yang, Graham C. Smith, and Haixue Yan. "Energy storage properties of samarium-doped bismuth sodium titanate-based lead-free ceramics." Chemical Engineering Journal 473 (2023) 145363.

[35] Hu, Zijun, Da Chen, Sen Wang, Ning Zhang, Laishun Qin, and Yuexiang Huang. "Facile synthesis of Sm-doped BiFeO3 nanoparticles for enhanced visible light photocatalytic performance." Materials Science and Engineering B. 220 (2017) 1-12.

[36] Pascu, Rovena Veronica, George Epurescu, Iulian Boerasu, Ana-Maria Banici Niculescu, Dumitru Manica, Alexandra Maria Isabel Trefilov, and Bogdan Alexandru Sava. "Samarium doped cerium oxide thin films deposited by pulsed laser deposition." Applied Surface Science. 606 (2022): 154994.

[37] Mohammadi, Alireza, Mohammad Kazemeini, and Samahe Sadjadi. "Synthesis and physicochemical evaluations of a novel MIL-101 (Fe)-PMA-Biochar triple composite photocatalyst activated through visible-light and utilized toward degradation of organic pollutants: optimal operations and kinetics investigations." Photochemical & Photobiological Sciences 22, no. 6 (2023): 1357-1378.

[38] Xiao, Qi, Zhichun Si, Jiang Zhang, Chong Xiao, Zhiming Yu, and Guanzhou Qiu. "Effects of samarium dopant on photocatalytic activity of TiO2 nanocrystallite for methylene blue degradation." Journal of materials science 42 (22) (2007) 9194-9199.

[39] Shi, Zhongliang, Hong Lai, and Shuhua Yao. "Preparation and photocatalytic activity of magnetic samarium-doped mesoporous titanium dioxide at the decomposition of methylene blue under visible light." Russian Journal of Physical Chemistry A. 86 (8) (2012) 1326-1331.

[40] Wulandari, Dwi Aprillia, Agustino Zulys, and Eny Kusrini. "Samarium complexes from 2, 6-Naphtalenedicarboxylate: synthesis, photocatalytic properties and degradation of methylene blue." In IOP conference series: materials science and engineering. 546 (4) (2019) 042050.

[41] Naveen, M. V., G. Krishnamurthy, T. C. M. Yuvaraj, R. Harini, T. Manjuraj, and G. Nagaraju. "Enhanced photocatalytic applications of Ce-doped MoO3 nanoparticles synthesized via combustion process using Calophyllum seed powder." Journal of Molecular Structure 1328 (2025): 141125.

[42] Khataee, Alireza, Shabnam Saadi, Behrouz Vahid, Sang Woo Joo, and Bong-Ki Min. "Sonocatalytic degradation of Acid Blue 92 using sonochemically prepared samarium doped zinc oxide nanostructures." Ultrasonics sonochemistry. 29 (2016) 27-38.

[43] Gracheva, Maria, Zoltán Homonnay, Amarjeet Singh, Ferenc Fodor, Vanda B. Marosi, Ádám Solti, and Krisztina Kovács. "New aspects of the photodegradation of iron (III) citrate: spectroscopic studies and plant-related factors." Photochemical & Photobiological Sciences 21, no. 6 (2022): 983-996.

[44] Shabbir, Mohsin, Muhammad Imran, Ali Haider, Iram Shahzadi, Wakeel Ahmad, Anwar Ul-Hamid, Walid Nabgan et al. "Efficient samarium-grafted-C3N4-doped α-MoO3 used as a dye degrader and antibacterial agent: in silico molecular docking study." ACS omega. 8 (38) (2023) 34805-34815.

[45] Jamshaid, Muhammad, Muhammad Imran Khan, Hasan M. Khan, Abdul Rauf, Ome Parkash Kumar, Muhammad Nadeem Akhtar, Shahid Iqbal, Abdallah Shanableh, and Aziz ur Rehman. "Sm-Co substituted M-type lead hexaferrite for dielectric properties and visible light driven methylene blue degradation in industrial wastewater." Desalination and water treatment. 226 (2021) 431-440.

[46] Zilabi, Sara, Sajjad Habibzadeh, Majedeh Gheytanzadeh, and Mohammad Rahmani. "Direct sunlight catalytic decomposition of organic pollutants via Sm-and Ce-doped BiFeO3 nanopowder synthesized by a rapid combustion technique." Catalysis Letters. 151 (12) (2021) 3462-3476.

[47] Bekena, Fekadu Tadesse, Dong-Hau Kuo, and Lalisa Wakjera Duresa. "Detoxification of organic pollutants over novel niobium and cobalt codoped molybdenum oxy-sulfide photocatalyst under visible light." Photochemical & Photobiological Sciences 25, no. 3 (2026): 437-451.

[48] El Rouby, W. M. A., A. A. Farghali, and A. Hamdedein. "Microwave synthesis of pure and doped cerium (IV) oxide (CeO2) nanoparticles for methylene blue degradation." Water Science and Technology 74 (10) (2016) 2325-2336.